4.2. Photovoltage decay

Fig. 3a displays a measure of the transient photovoltage signal during and after the laser pulse taken in the free-run mode on p-type silicon. It was obtained by tuning the CMA to a kinetic energy on the high energy side of the 2p core level, where there is significant slope, and allowing the TDC to histogram photoelectron arrival times for 1.3×10^7 laser shots, or about one-half hour. (This is a factor of four longer than typical data acquisition.) Also shown, in fig. 3b, is the system time resolution function plotted using the same time scale as the data. Free-run mode benefits from multibunch operation where the average ring currents are larger. It also allows all times to be interrogated and averages out the substantial pulse-to-pulse intensity variations seen in multibunch operations, a great convenience for on-line data interpretation. For fig. 3, the CMA was operated at 50 eV pass energy in the interest of time resolution (15 ns) and signal-to-noise considerations. The concomitant poor energy resolution (300 meV) is actually helpful when one is converting the raw counts of fig. 3a into true photovoltage by fitting the EDC count rate versus energy to a smoothly varying function. (This function is then used to convert the count rate versus time of fig. 3a into energy versus time.) A reduced energy resolution also increases dynamical range for large photovoltage shifts since the slope of the EDC is spread out over a larger energy. Of course with too poor an energy resolution, the slope is reduced to the point were signal-to-noise suffers. The scheme just described for converting a TDC histogram into photovoltage only works if the EDC experiences a rigid shift with no shape changes. This assumption is readily checked by data such as that in fig. 1 and in fact was found to be invalid for spectra at lower kinetic energy where laser induced amplitude changes in the secondaries occurred.

Although the TDC had only 1 ns indeterminacy, it was frequently necessary to degrade this with the histogramming scheme in order to reduce the memory to record a histogram of long duration. For programming convenience we chose to histogram directly into a low-memory 16 kbyte Fortran integer array which, in the DEC LSI architecture, significantly taxes memory available for the acquisition program. The data of fig. 3a were recorded with 4 ns time bins over a 32 μs window. Other combinations used were 1 ns over 8 μs, 2 ns over 16 μs, and 8 ns over 64 μs.

At high count rates, it is possible to exhaust the 8 hit capacity of the TDC before the data window of interest is closed. For example, at a 200 kHz count rate, photoelectron pulses are arriving with a mean separation of 5 μs, which on average will fill up the TDC hit registers within 40 μs. This causes the TDC to exhibit an effec-

tive dead time which gets worse the longer it it active. For a *constant* count rate, the TDC histogram droops at later times with a functional form given by

$$C = e^{-\Gamma t} \sum_{n=0}^{N-1} \frac{1}{n!} (\Gamma t)^n, \qquad (2)$$

where C is the accumulated counts, t is the time since the data window was opened, N is the maximum number of hits the TDC will accommodate, and Γ is the photoelectron count rate. Eq. (2) was derived from a consideration of Poisson statistics. For varying count rates such as occur in fig. 3a, a numerical scheme will be necessary to correct the data for histogram droop, if required. The droop can be reduced by cascading TDCs. This requires home made external circuitry to hold off the second TDC until the first fills up and to prevent the arrival of hits when the extended readout time overruns the next laser pulse. (A dedicated in-crate CAMAC processor could speed up TDC readout and histogramming significantly and would reduce the number of overrun laser shots.) A multihit TDC of sufficient capacity and equipped for automatic histogramming into in-crate memory could alleviate droop problems but is not commercially available.

Acknowledgements

This project could not have been executed without the help of many individuals and the NSLS staff. Within our PRT, important contributions were made by J.C. Rife, M.N. Kabler, H.R. Sadeghi, and J.D. Cassidy. Among the NSLS staff, special thanks go to John Keane for providing the ring rf signal, and Ben Craft for his sympathetic attitude in providing single bunch operation during studies at a time when no formal procedure for accommodating special operations was in place at NSLS.

References

[1] J.M. Bizau, D. Cubaynes, P. Gerard, F.J. Wuilleumier, J.L. Picque, D.L. Ederer, B. Carre and G. Wendin, Phys. Rev. Lett. 57 (1986) 306.
[2] V. Saile, Appl. Opt. 19 (1980) 4115.
[3] W. Eberhardt, R. Brickman and A. Kaldor, Solid State Commun. 42 (1982) 169.
[4] A. Ishizaka and Y. Shiraki, J. Electrochem. Soc.: Electrochemical Science and Technology 133 (1986) 666.
[5] W.R. Hunter, R.T. Williams, J.C. Rife, J.P. Kirkland and M.N. Kabler, Nucl. Instr. and Meth. 195 (1982) 141.
[6] M.M. Traum and D.P. Woodruff, J. Vac. Sci. Technol. 17 (1980) 1202.

Section V. Research applications

NEW TRENDS IN X-RAY STANDING WAVES

Michael J. BEDZYK

School of Applied and Engineering Physics and Cornell High Energy Synchrotron Source, Cornell University, Ithaca, New York 14853, USA

A review of three new methods for generating X-ray standing waves is given, namely Bragg diffraction from layered synthetic microstructures, specular reflection from mirror surfaces, and Bragg diffraction in the backscattering geometry. Unlike conventional X-ray standing wave measurements which use dynamical Bragg diffraction from perfect single crystals (such as silicon and germanium), these new methods provide angular reflection widths measured in milliradians instead of microradians and are therefore applicable to a more general class of solid substrates. Emphasis will be given to the application of these new methods for the study of surface and interface structures.

1. Introduction

The interference between two coherently coupled X-ray travelling plane waves generates an X-ray standing wave field, which in turn produces anomalies in the photoeffect cross section for atoms distributed within the interference field. In 1964 Batterman [1] made the first observation of this phenomenon by monitoring the germanium K fluorescence while rocking a perfect single crystal of Ge through the (220) Bragg diffraction condition. In later demonstrations, Golovchenko and co-workers [2] used standing waves extending out from the surface of silicon single crystals to determine the registration of surface impurity atoms with respect to the underlying bulk diffraction planes.

In these "conventional" standing wave measurements, dynamical Bragg diffraction from single crystals in the reflection geometry was used to generate an X-ray standing wave with a period equivalent to the d-spacing. Referring to fig. 1, on the low angle side of the Bragg reflection the nodes of the standing wave coincide with the diffraction planes. As the Bragg angle is advanced through the rocking curve the standing wave moves in a continuous fashion inward by one-half of a diffraction plane spacing. Since the photoelectric effect is (by the dipole approximation) proportional to the E field intensity at the center of an atom, this precise movement of the standing wave produces modulations in the photoeffect yield from an atomic species. The phase and amplitude of this modulation (or the so-called coherent position and coherent fraction) are a measure of the mean position $\langle z \rangle$ and width $\langle z^2 \rangle^{1/2}$ of the atom distribution within the unit d-spacing. A more detailed description of this relationship is given in ref. [3].

With very narrow reflectivity widths of a few arc-sec-

onds, these conventional standing wave measurements required the use of highly perfect single crystals (such as Si and Ge). Bragg diffracted plane waves from less perfect crystals would have low intensities in comparison to the incident intensity and therefore the resulting standing wave would have a very weak and indistinct modulation amplitude. Needless to say, the requirement of perfect single crystals limited the application of this otherwise very powerful technique. In recent demonstrations, however, this limiting feature has been overcome by the development of three new methods for generating X-ray standing waves. These are: (1) the use of Bragg diffraction from layered synthetic microstructures; (2) the use of specular reflection from a mirror surface; and (3) the use of Bragg diffraction at Bragg angles near 90°. Each of these new X-ray standing wave methods has a natural resonant width measured in
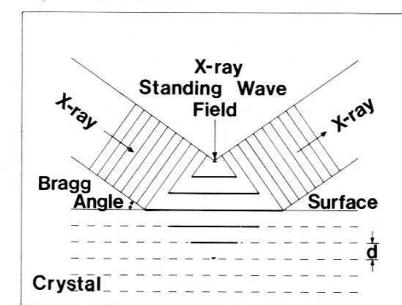

Fig. 1. Illustration of the X-ray standing wave field formed by the interference between the incident and Bragg diffracted plane waves.

milliradians rather than microradians and is therefore less sensitive to crystal imperfections.

2. Layered synthetic microstructures

The first of these new standing wave methods was the use of Bragg diffraction from a layered synthetic microstructure (LSM) by Barbee and Warburton [4]. For Bragg diffraction applications LSMs are made periodic with alternating layers of high and low electron density materials, such as platinum and carbon. These LSMs are produced with a fundamental period or diffraction plane spacing ranging from 15 to 200 Å and with 10 to 200 layer pairs. Due to the low number of layer pairs which effect Bragg diffraction, these optical elements have a rather large energy bandpass and Bragg reflection width. Details describing the Bragg diffraction properties of LSMs are given elsewhere [5–7]. The essential point is that experimental reflection curves from LSMs compare well with predictions from dynamical diffraction theory, and peak reflectivities are as high as 80%. Therefore a well defined standing wave pattern can be produced and used to probe for structures deposited on the LSM surface with a periodic scale equivalent to the d-spacing.

With the capability of being able to choose both the standing wave period and material composition used in the multilayer, this technique has great potential for resolving various surface and interface structures. At CHESS we have recently employed this LSM standing wave technique for studying electrochemical interfaces [8] and lipid bilayers [9].

The electrochemical system that we studied involved the adsorption of a layer of iodide onto a platinum surface, followed by the electrodeposition of a layer of copper. The LSM (furnished by T.W. Barbee of Lawrence Livermore Laboratory) consisted of 15 platinum–carbon layer pairs with platinum as the outermost layer. The thickness of the platinum and carbon layers were 26 and 30 Å, respectively ($d = 56$ Å). The layers were grown by a sputter deposition technique on a flat silicon (111) substrate. At 9.2 keV the incident X-rays induced L-level and K-level fluorescence from the iodine and copper, respectively. The fluorescence yields collected with an energy dispersive solid state detector along with the reflected intensity from the LSM are shown in fig. 2 for a scan in angle θ through the first order Bragg peak. The crucial feature in this result is the noticeable phase difference between the modulations of the iodine and copper fluorescence yields, with the copper maximum shifted to the high angle side of the iodine maximum. Since the antinode of the standing wave moves inward as the angle is increased, the order in which these maxima occur indicates that the copper layer lies in between the iodide
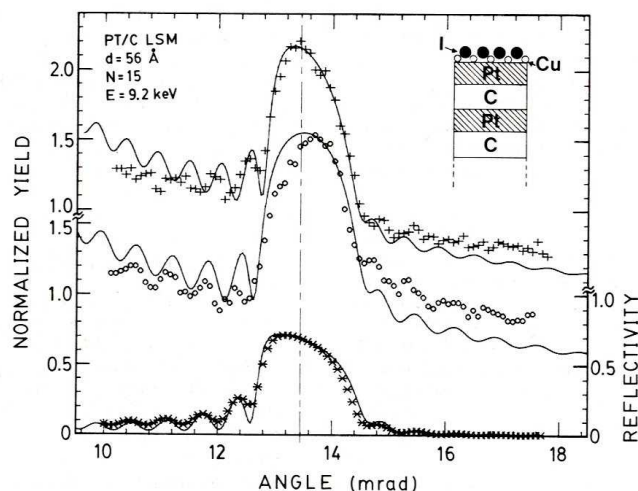
layer and the surface of the platinum as illustrated in the inset of fig. 2. This is quite significant, since it shows that the predeposited iodide layer was displaced from the platinum surface by the electrochemically deposited copper. From the theoretical fits shown in fig. 2, we conclude that the Cu and iodide layers are separated by 3.3 Å. (The coverage for each layer was approximately 6×10^{14} atoms/cm^2.)

3. Specular reflection

Under the specular reflection condition the incident and specular travelling plane waves interfere to form a standing wave in the more optically dense medium above the mirror surface. At the same time, travelling wave solutions are forbidden below the mirror surface, and an evanescent or exponentially damped wave is formed which penetrates only a short distance into the less optically dense medium. This is illustrated in fig. 3 where a depth profile of the E field intensity above and below the reflecting interface of a carbon coated platinum mirror is shown for incident angles at, above, and below the critical angle. A corresponding specular reflection curve can be found in fig. 4. At $\theta = 0$ a node is at the mirror surface and the first antinode is at infinity; as the incident angle θ is increased the first antinode moves inward until at the critical angle θ_c it coincides with the mirror surface. The trailing antinodes follow behind with a periodic spacing of $\lambda/(2 \sin \theta)$ in vacuum.

Fig. 2. Experimental data and theoretical curves for the Bragg reflectivity (∗), copper K fluorescence (○), and iodine L fluorescence (+) as a function of angle θ for a Pt/C LSM covered with an electrodeposited layer of Cu atoms and an adsorbed layer of iodine atoms. The incident X-ray energy was 9.2 keV.
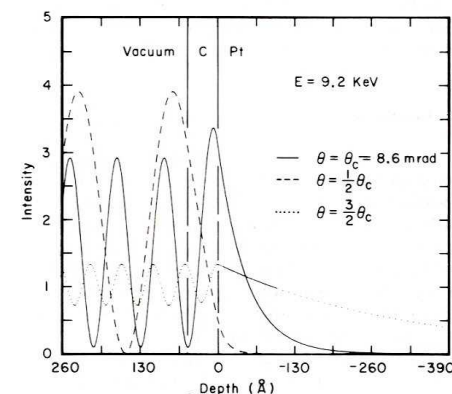
Fig. 3. Theoretical depth profiles for the E field intensity above and below the surface of a platinum mirror which is coated with a 60 Å thick carbon film. The incident X-ray energy is 9.2 keV. The solid line corresponds to the depth profile at the critical angle $\theta_c = 8.6$ mrad, the dashed line corresponds to $\theta = \theta_c/2$, and the dotted line corresponds to $\theta = 3\theta_c/2$.
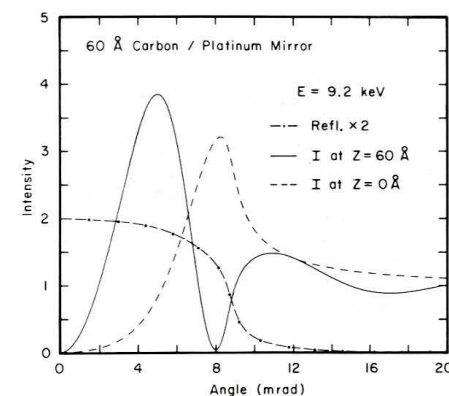
Fig. 4. Theoretical specular reflectivity and E field intensity curves vs incident angle for the carbon coated platinum mirror described in fig. 3. The dash–dot curve corresponds to twice the reflectivity, the solid curve corresponds to the E field intensity on top of the 60 Å thick carbon layer, and the dashed curve corresponds to the E field intensity at the C/Pt interface.

Although much attention has been given to the evanescent-wave [4,10–12] (with applications to surface diffraction and surface enhanced fluorescence), little or no attention has been paid to using the long-period standing wave as a structure probe. Such a probe would be ideal for studying a system in which a plane of heavy atoms is displaced outward from a mirror surface by a low-Z material tens of ångströms thick. Referring to the example in figs. 3 and 4, a heavy atom placed on top of the 60 Å thick carbon film would sense a modulation of the E-field intensity as described in fig. 4 (I at $z = 60$ Å). Note that this length of a displacement outward receives a full modulation of the E field intensity in contrast to the incomplete modulation sensed at the C/Pt Interface (I at $z = 0$ Å).

In a recent study [9] we have used both the specular reflection and LSM standing wave techniques to characterize the thermotropic hydrocarbon order/disorder transition in soap films. The length of the hydrocarbon chains fully extended at room temperature placed the heavy atom layer from the head group of these chains out far enough from the mirror surface so that we could observe a full modulation of the fluorescence yield from the heavy atom layer.

4. Backscattering Bragg diffraction

Based on conventional dynamical diffraction theory [13,14], the angular width for the strong Bragg diffrac-
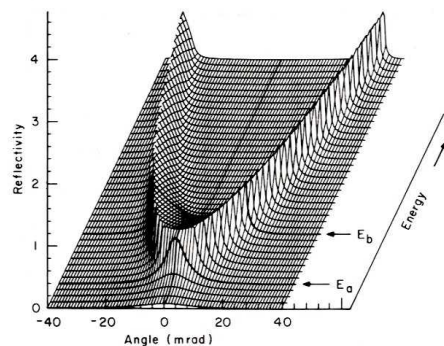
V. RESEARCH APPLICATIONS

Fig. 5. Theoretical Pt(222) Bragg reflection profiles in the neighborhood of $\theta_B \cong \pi/2$ rad. The angle scale is referenced to the surface normal direction. The curve labelled E_a corresponds to an incident energy of $E_a = 5.4720173$ keV. Each subsequent curve is given a 0.1 vertical scale offset and a 87.8 meV increment in energy.

tion condition in the reflection geometry (i.e. the Darwin width) is expressed as:

$$W = 2|P|\Gamma F_h / (|b|^{1/2} \sin 2\theta_B). \qquad (1)$$

(The definition of the various parameters used in this notation can be found in ref. [14].) Since the average dielectric susceptibility ($\chi_0 = -\Gamma F_0$) has a typical value of $\sim 10^{-5}$ for X-rays in solids, conventional Bragg widths are typically between 10 and 100 μrad. Therefore a weak standing wave would be generated by conventional Bragg diffraction from a single crystal with a 1 mrad mosaic spread.

For $\theta_B > 88°$ the conventional theory and this expression for the width break down. This is due to an approximation which treats the spherical asymptotes of the dispersion surface as planes. Using an extended dynamical diffraction theory, the Bragg reflectivity [15–18] and standing wave intensity [19] can be properly described in this backscattering regime ($87° < \theta_B < 90°$) by approximating the spherical asymptotes as paraboloids. Referring to the 3-dimensional DuMond plot shown in fig. 5, the Bragg reflectivity has a very small energy width and broad angle width in this region. The largest angle width occurs at a wavelength of

$$\lambda_b = 2d(1 - \Gamma(F_0' + F_h')/2).$$

This marks the point at which the β branch of the dispersion surface disappears. For energies above this β branch cutoff point labelled E_b, the angular width can be expressed as:

$$W = \Delta\theta_{y=1} - \Delta\theta_{y=-1}, \qquad (2)$$

where $\Delta\theta_{y=1}$ and $\Delta\theta_{y=-1}$ refer to the angular displacements from 90° of the low and high angle side of the strong Bragg diffraction condition, respectively. For a symmetric reflection

$$\Delta\theta_{y=\pm1} = [2(1 - \sin\theta_B) + \Gamma(-F_0' \pm F_h')]^{1/2}, \qquad (3)$$

where $\sin\theta_B = \lambda/2d$. For energies below E_b and above E_a:

$$W = \Delta\theta_{y=1}. \qquad (4)$$

The incident photon energy, labelled E_a in fig. 5, corresponds to

$$\lambda_a = 2d(1 - \Gamma(F_0' - F_h')/2).$$

Strong Bragg diffraction does not occur below this energy, since this marks the point at which the gap between the dispersion surfaces disappears.

For the Pt(222) Bragg reflection chosen as an example in fig. 5, $d = 1.133$ Å, $F_0 = 293.7 + i50.3$, $F_h = 168.5 + i47.1$, and $\Gamma = 7.617 \times 10^{-7}$ at $E = 5.472$ keV. Using eqs. (2) and (3), the angular width at $E_b = 5.47272$ keV is 16.02 mrad. The energy width for this reflection at 90° is $E_b - E_a = 0.702$ eV. In general the energy bandwidth is

$$\Delta E/E = \Gamma F_h' \qquad (5)$$

for backscattering Bragg diffraction.

Using soft X-rays, Ohta et al. [20] have used standing waves in the backscattering mode to study the UHV clean Si(111) surface. More recently Woodruff et al. [21] have shown how such standing waves can be employed to study chlorine adsorbed on a Cu(111) crystal with a mosaicity of tenths of degrees. In both of these cases an EXAFS type monochromator was used to scan the energy through the 90° Bragg diffraction condition.

5. Conclusion

With the means of generating X-ray standing waves on a more general class of substrates, we are now in a position to apply the X-ray standing wave technique to a large variety of surface and interface structures. Included in this list would be the standing wave analysis of lipid bilayers and liquid/solid electrochemical interfaces. We are presently applying the backscattering Bragg diffraction standing wave method to the study of Cu electrodeposited on an iodide passivated Pt(222) surface [22]. The positional information from this will be complimentary to the LSM standing wave work described in fig. 2, since the position will be measured on a d-spacing scale of 1.133 Å rather than 56 Å. By combining this higher resolution measurement with the lower resolution LSM result, it will be possible to more accurately determine the registration of this adsorbate system with respect to the underlying Pt surface atom arrangement.

References

[1] B.W. Batterman, Phys. Rev. 133 (1964) A759.
[2] P.L. Cowan, J.A. Golovchenko and M.F. Robbins, Phys. Rev. Lett. 44 (1980) 1680; J.A. Golovchenko, J.R. Patel, D.R. Kaplan, P.L. Cowan and M.J. Bedzyk, Phys. Rev. Lett. 49 (1982) 560.
[3] M.J. Bedzyk and G. Materlik, Phys. Rev. B31 (1985) 4110.
[4] T.W. Barbee and W.K. Warburton, Mater. Lett. 3 (1984) 17.
[5] L.G. Parratt, Phys. Rev. 95 (1954) 359.
[6] J.H. Underwood and T.W. Barbee, AIP Conf. Proc. No. 75 on Low Energy X-ray Diagnostics (1981) p. 170.
[7] D.H. Bilderback, B.M. Lairson, T.W. Barbee, G.E. Ice and C.J. Sparks, Nucl. Instr. and Meth. 208 (1983) 251.
[8] M.J. Bedzyk, D. Bilderback, J. White, H.D. Abruña and M.G. Bommarito, J. Phys. Chem. 90 (1986) 4926.
[9] M.J. Bedzyk, D. Bilderback, M.G. Bommarito, M. Caffrey and J. Schildkraut, unpublished.
[10] W.C. Marra, P. Eisenberger and A.Y. Chou, J. Appl. Phys. 50 (1979) 6927.
[11] R.S. Becker, J.A. Golovchenko and J.R. Patel, Phys. Rev. Lett. 50 (1983) 153.
[12] J.M. Bloch, M. Sansone, F. Rondelez, D.G. Peiffer, P. Pincus, M.W. Kim and P. Eisenberger, Phys. Rev. Lett. 54 (1985) 1039.
[13] M. von Laue, Roentgenstrahlinterferenzen (Akademische Verlagsgesellschaft, Frankfurt a.M., 1960).
[14] B.W. Batterman and H. Cole, Rev. Mod. Phys. 36 (1961) 681.
[15] K. Kohra and T. Matsushita, Z. Naturforsch. 27a (1972) 484.
[16] O. Brummer, H.R. Hoche and J. Nieber, Phys. Status Solidi A53 (1979) 565.
[17] A. Caticha and S. Caticha-Ellis, Phys. Rev. B25 (1982) 971.
[18] W. Graeff and G. Materlik, Nucl. Instr. and Meth. 195 (1982) 97.
[19] M.J. Bedzyk, Ph.D. Thesis, Physics Deptartment SUNY, Albany (1982).
[20] T. Ohta, Y. Kitajima, H. Kuroda, T. Takahashi and S. Kikuta, Nucl. Instr. and Meth. A246 (1986) 760.
[21] D.P. Woodruff, D.L. Seymour, C.F. McConville, C.E. Riley, M.D. Crapper, N.P. Prince and R.G. Jones, Phys. Rev. Lett. 58 (1987) 1460.
[22] M.J. Bedzyk, M. McMillan, J. White, M. Albarelli and H.D. Abruña, unpublished.